Journal of Nuclear Materials 502 (2018) 113–122

Contents lists available at ScienceDirect

Journal of Nuclear Materials

journal homepage: www.elsevier.com/locate/jnucmat

Comparison of structure, morphology, and leach characteristics of multi-phase ceramics produced via melt processing and hot isostatic pressing

Christopher S. Dandeneau [a, *], Tao Hong [b], Kyle S. Brinkman [b], Eric R. Vance [c], Jake W. Amoroso [a]

[a] Savannah River National Laboratory, Aiken, SC 29808, USA
[b] Department of Materials Science and Engineering, Clemson University, Clemson, SC 29634, USA
[c] Australian Nuclear Science and Technology Organisation, Lucas Heights, NSW 2234, Australia

HIGHLIGHTS

- Melt-processed and hot isostatically pressed (HIP) multi-phase waste forms produced.
- Significant differences in structure, morphology, and leach behavior observed.
- HIP temperature found to have substantial effect on sample properties.
- Melt processed sample exhibited lowest release rate for Cs and Rb.
- Hot isostatically pressed specimens showed greater Sr and Mo retention.

ARTICLE INFO

Article history:
Received 10 October 2017
Received in revised form
29 January 2018
Accepted 3 February 2018
Available online 8 February 2018

ABSTRACT

Melt processing of multi-phase ceramic waste forms offers potential advantages over traditional solid-state synthesis methods given both the prevalence of melters currently in use and the ability to reduce the possibility of airborne radionuclide contamination. In this work, multi-phase ceramics with a targeted hollandite composition of $Ba_{1.0}Cs_{0.3}Cr_{1.0}Al_{0.3}Fe_{1.0}Ti_{5.7}O_{16}$ were fabricated by melt processing at 1675 °C and hot isostatic pressing (HIP) at 1250 and 1300 °C. X-ray diffraction analysis (XRD) confirmed hollandite as the major phase in all specimens. Zirconolite/pyrochlore peaks and weaker perovskite reflections were observed after melt processing, while HIP samples displayed prominent perovskite peaks and low-intensity zirconolite reflections. Melt processing produced specimens with large (>50 μm) well-defined hollandite grains, while HIP yielded samples with a more fine-grained morphology. Elemental analysis showed "islands" rich in Cs and Ti across the surface of the 1300 °C HIP sample, suggesting partial melting and partitioning of Cs into multiple phases. Photoemission data revealed multiple Cs 3*d* spin-orbit pairs for the HIP samples, with the lower binding energy doublets likely corresponding to Cs located in more leachable phases. Among all specimens examined, the melt-processed sample exhibited the lowest fractional release rates for Rb and Cs. However, the retention of Sr and Mo was greater in the HIP specimens.

1. Introduction

Waste generated from the reprocessing of commercial used nuclear fuel (UNF) is conventionally immobilized in borosilicate glasses. The volume of research devoted to refinements in the vitrification of glass waste forms, and the resulting number of technological advancements achieved, have far outpaced those associated with other methods of waste immobilization [1]. However, certain fission products (e.g., Mo, Ru) and actinides have limited solubility in borosilicate glass waste forms [1,2]. Furthermore, when exposed to the geothermal actions of water and/or humid air, glass waste forms have the potential to corrode, leading to the release of high level waste (HLW) elements into the

* Corresponding author.
E-mail address: christopher.dandeneau@srnl.doe.gov (C.S. Dandeneau).

https://doi.org/10.1016/j.jnucmat.2018.02.006
0022-3115/

biosphere [3]. The consequences of such a scenario have spurred research into the development of alternative waste forms, including multi-phase ceramics capable of immobilizing waste elements in durable (i.e., leach resistant) crystalline matrices.

Among the most extensively studied phase assemblages for use as a ceramic waste form is the SYNROC (i.e., synthetic rock) family of titanate ceramics, the design of which is built on the concept of simulating naturally occurring minerals that have immobilized radionuclides over geologic timescales [4–8]. The primary host for alkali metals, namely Cs and Rb, in SYNROC is the hollandite phase with the general formula $Ba_xCs_y(M^{3+})_{2x+y}Ti_{8-2x-y}O_{16}$, where M is a trivalent transition metal cation [9]. Sets of edge-sharing $(M^{3+},Ti)O_6$ octahedra in hollandite are joined at the corners to other edge-sharing octahedra, resulting in the formation of tunnels capable of accommodating large alkali/alkaline earth elements [10]. The size of these tunnels is heavily influenced by the ionic radii of trivalent cations occupying octahedral sites; the substitution of M^{3+} cations into the hollandite lattice (or the reduction of Ti^{4+} to Ti^{3+} during processing) has been shown to expand the tunnel size and facilitate Cs incorporation [11]. Furthermore, the ability of the hollandite structure to accommodate ^{137}Cs transmutation to ^{137}Ba via beta-decay can be achieved through the reduction of Ti^{4+} to Ti^{3+} [12,13].

The target phases for the immobilization of Zr and actinides in SYNROC are zirconolite ($CaZrTi_2O_7$) and pyrochlore ($A_2B_2O_7$), both of which are anion-deficient derivatives of the fluorite structure [14–17]. The structure of monoclinic zirconolite-2M can be derived by compression of the pyrochlore lattice along the [111] direction [18,19]. While the capacity of lanthanides to form titanate pyrochlores is widely known, lanthanide substitution may also occur at Ca sites in zirconolite, with charge balance being maintained by the substitution of M^{3+} ions at $(Ti/Zr)^{4+}$ sites [20,21]. Furthermore, it has been reported that the introduction of multivalent actinide surrogates (e.g., Ce) facilitates transitions between different zirconolite polymorphs [22]. Immobilization of both lanthanides and alkaline earth metals is further achieved in SYNROC by targeting the formation of perovskite (ABO_3) phases [3,23]. It is noted that perovskite and pyrochlore phases have been shown to form by the partitioning of zirconolite after extensive lanthanide loading [24].

Due to the high volatility of Cs, SYNROC-type assemblages are often fabricated via hot isostatic pressing (HIP) [25]. However, recent efforts have been focused on designing compositions based on a simulated waste stream that, when combined with suitable additives and melted, form crystalline hollandite, zirconolite, perovskite, and pyrochlore phases [26]. The multi-phase nature of these melt-processed ceramics allows for a broad range of different waste elements to be incorporated into tailored crystal structures, thereby providing an opportunity to broaden the available disposal options and lower waste treatment costs. Furthermore, the utilization of melters by several countries for the vitrification of HLW enhances the technological readiness of melt processing for multi-phase ceramic waste form production [27]. When fabricating the waste forms, melt processing can also utilize liquid feeds, which reduce the potential for airborne radionuclide contamination (e.g. dusting) compared to traditional solid-state synthesis protocols.

The immobilization of Cs by incorporation into hollandite is one of the more difficult tasks encountered when melt processing multi-phase ceramics in air. In addition to its high-temperature volatility, Cs has a tendency to form water-soluble secondary phases and thus, the formulation of proper targeted hollandite stoichiometries is critical. Previous research on melt-processed ceramics has indicated that Cr plays a role in stabilizing the hollandite phase and promoting Cs incorporation into the structure [26,28]. As a consequence of its refractory nature, Cr does not readily form Cs compounds, and the Cr^{3+} ion is not prone to reduction. While Cr doping has been demonstrated to improve Cs immobilization in melt-processed ceramic waste forms, this work represents the first direct comparison of the structure and properties of melt-processed and HIPed multi-phase ceramics with the same target phase assemblage and Cr-doped hollandite composition.

In this study, multi-phase ceramic waste forms with identical targeted phase assemblages were produced via melt processing and HIP techniques. An investigation into the structure, morphology, elemental speciation characteristics, and leach behavior of the ceramics was subsequently conducted. It is expected that the findings of this research will facilitate the future development of both optimized processing protocols and more durable (i.e., leach-resistant) multi-phase ceramic waste forms.

2. Experimental procedure

2.1. Composition development

The targeted waste form composition investigated in this work was developed at Savannah River National Laboratory (SRNL) based on simulated waste streams devised as part of the Fuel Cycle Research and Development (FCR&D) program initiated by the United States Department of Energy (DOE) [26,29–32]. A multi-phase ceramic with a target hollandite stoichiometry of $Ba_{1.0}Cs_{0.3}Cr_{1.0}Al_{0.3}Fe_{1.0}Ti_{5.7}O_{16}$ (hereafter referred to as CAF-131) was batched and used as the baseline composition in this work. The targeted weight percentages of the different phases were 65.4% hollandite, 14.61% zirconolite, 16.84% pyrochlore, 2.54% perovskite, and 0.61% metal. Targeted oxide concentrations for the baseline CAF-131 composition are given in Table 1.

2.2. Processing and fabrication

Batch material in this work was prepared by mixing stoichiometric amounts of oxide and carbonate powders in 500 mL plastic bottles with zirconia milling media. The bottles were filled to approximately two-thirds capacity with deionized water and then agitated in a tumbler mixer for 30 min. Upon removal from the mixer, the resulting slurry was poured into stainless steel pans and allowed to dry for 24 h at 90 °C. The dried material was ultimately utilized as feed stock in both melt processing and HIP procedures.

For the melt-processed sample, a Pt/10%Rh crucible containing 100 g of feed stock for the targeted composition was covered with an alumina lid and loaded into a furnace. The furnace was then heated from room temperature to approximately 1675 °C at a rate of ~5 °C/min. After a dwell time of 20 min, the lid was removed and the temperature in the furnace was allowed to re-equilibrate (pouring is not possible if the lid remains in place, as the melt will solidify during the time it takes to remove the lid and attempt to pour the material). The contents of the crucible were subsequently poured into a stainless steel mold Once the melt had cooled and solidified, the crystallized material was stored for further analysis.

A portion of the CAF-131 feed stock was transferred to the Australian Nuclear Science and Technology Organization (ANSTO) and subjected to HIP treatments at temperatures of 1250 and 1300 °C; these specimens are denoted as HIP-1250 and HIP-1300. Prior to HIPing, the feed stock was calcined at 850 °C for 4 h in air. Numerous studies on hollandite have shown that the addition of Ti metal powder before HIPing is an effective means of controlling redox conditions and preventing the formation of water-soluble Cs_2MoO_4 by reducing Mo^{6+} to lower valence states [33–35]. Ti metal also reacts with TiO_2 to produce Ti^{3+} cations, which are then incorporated into the hollandite to facilitate Cs immobilization [9,34]. In this work, 5 wt% Ti metal was added to the

Table 1
Targeted oxide concentrations for the baseline CAF-131 composition.*

Component Oxide	Targeted wt%	Component Oxide	Targeted wt%
Al_2O_3	1.27	Cs_2O	2.88
CaO	1.39	La_2O_3	1.58
CdO	0.11	MoO_3	0.85
Cr_2O_3	6.33	Nd_2O_3	5.23
Eu_2O_3	0.17	Pr_2O_3	1.45
Fe_2O_3	6.65	SeO_2	0.08
Gd_2O_3	0.16	SnO_2	0.07
SrO	0.98	Sm_2O_3	1.08
TiO_2	49.16	TeO_2	0.66
ZrO_2	2.99	Y_2O_3	0.63
BaO	12.76	Rb_2O	0.42
Ce_2O_3	3.10		

*The additive oxides are shaded green. The remaining oxides comprise the waste. BaO is part of the waste stream, but additional BaO is added to form stoichiometric hollandite.

calcined oxide mixture before HIPing; the introduction of Ti metal also enables comparisons with previous research. The material was subsequently loaded into stainless steel canisters and heated in an Ar atmosphere for 2 h under a pressure of 100 MPa. The densified specimens were ultimately sent back to SRNL for characterization.

2.3. Phase/elemental identification and microstructural characterization

X-ray Diffraction (XRD) patterns were collected to identify the constituent phases in both melt-processed and HIP samples. The patterns were obtained with a Bruker D8 Advance instrument, while phase identification was performed using the JADE software package. Scanning Electron Microscopy (SEM) images and Energy-Dispersive Spectroscopy (EDS) analysis were conducted to investigate microstructural characteristics and elemental speciation in the specimens. SEM images and elemental maps were acquired with a Hitachi SU6600 instrument at the Advanced Materials Research Laboratory of Clemson University; a total sum of 100 at% was assumed for all metallic species when quantifying the EDS results, as the presence of oxygen was detected in all mapping and point scans. Photoemission data were obtained with a Kratos AXIS Ultra DLD X-ray photoelectron spectroscopy (XPS) system utilizing a monochromatic Al Kα source; the take-off angle was 45°. The binding energies were calibrated using the C 1*s* peak at 284.8 eV as a reference. Deconvolution of the XPS spectra was performed with CasaXPS Version 2.3.18 software.

2.4. Leach testing

The durability of the fabricated ceramics was evaluated by 28-day monolith leach tests conducted according to a modified version of Matrix C in the ASTM C1220-10 standard [36]. Monolithic rectangular specimens were polished on their faces with 600 grit SiC paper and placed on Teflon supports positioned at the bottom of 22 mL stainless steel pressure vessels. The vessels were filled with ASTM Type I water collected from an ARIES High Purity Water System (resistivity greater than 18 MΩ cm), sealed with threaded steel closure fittings, and placed into an oven maintained at a constant temperature of 90 ± 2 °C; the ratio of the specimen surface area to leachant volume was 5.9. Surface area was determined according to geometric dimensions measured with a digital caliper accurate to within ±0.02 mm. Leachate volumes of 0.5 mL were sampled from each vessel after 1, 7, 14, and 28 days. Water was not added to replace the leachate volume removed (i.e., the final leachate volume was 2 mL less than when the test started). Inductively Coupled Plasma-Mass Spectroscopy (ICP-MS) was employed to measure elemental concentrations in the leachates and the initial concentration of Cs. Aside from Cs, the elemental content in the as-processed (i.e., before leach testing) samples was measured via Inductively Coupled Plasma-Atomic Emission Spectroscopy (ICP-AES). Specimens for analysis were prepared by both sodium peroxide and lithium metaborate fusion methods; data were collected in duplicate for each element of interest. The fractional release rate of element *i* in each specimen (FR_i) was determined according to the following equation:

$$FR_i = \frac{C_i V_s}{f_i m_s} \quad (1)$$

where C_i is the concentration of element *i* in the leachate (g/L), V_s is the leachate volume (L), f_i is the fraction of element *i* in the as-processed, unleached specimen (unitless), and m_s is the sample mass (g).

3. Results and discussion

3.1. XRD analysis

Shown in Fig. 1 are the XRD patterns of CAF-131, HIP-1250, and HIP-1300. As stated above, these specimens were fabricated from identical feed stock mixtures. The patterns from all samples show strong reflections corresponding to the hollandite phase. However, as evident in the inset, the hollandite peaks for HIP-1250 and HIP-1300 are shifted to lower 2θ angles. Considering the Bragg relation ($n\lambda = 2d\sin\theta$, where *n* is an integer, λ is the wavelength of incident X-rays, *d* is the interplanar spacing, and θ is the diffraction angle), a higher content of large Cs and Rb cations in the hollandite phase serves to increase the interplanar spacing and, since $n\lambda$ is constant, a shift in the hollandite peaks to lower 2θ angles would be observed; such a phenomenon has been reported in previous work [37,38]. The above scenario is supported by ICP-MS data obtained for the as-processed samples (Table 2). For CAF-131, the high temperature (1675 °C) needed to melt the feed stock led to a loss of

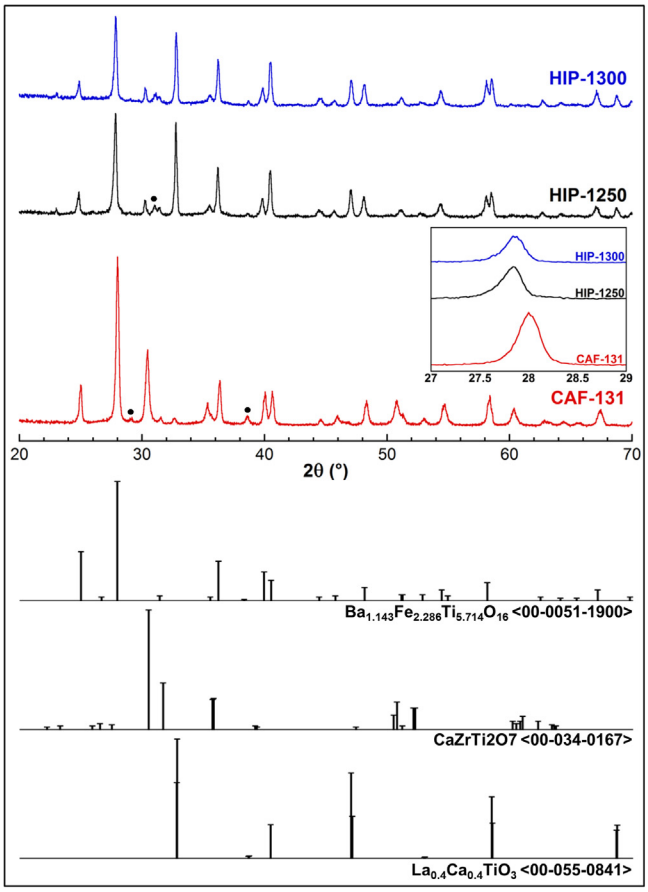

Fig. 1. XRD patterns obtained for CAF-131, HIP-1250, and HIP-1300; the hollandite peak of maximum intensity ($2\theta = 27–29°$) is shown in the inset. The reference peaks used to identify hollandite, zirconolite, and doped perovskite phases are displayed from top to bottom below the patterns; ● indicates pyrochlore-type phases.

Table 2
Target and measured elemental compositions for melt-processed and HIPed samples.[a]

Element	T[a]rget (wt%)	Measured Concentrations (wt%)		
		CAF-131	HIP-1250	HIP-1300
Al	0.67	0.72	0.64	0.65
Ba	11.43	11.05	9.94	10.08
Ca	0.99	1.09	1.17	1.17
Cd	0.10	<0.10	<0.10	<0.10
Ce	2.65	1.78	2.69	2.68
Cr	4.33	4.37	4.35	4.36
Cs	2.72	0.8	2.45	2.4
Eu	0.15	0.14	0.11	0.12
Fe	4.65	5.26	4.69	4.64
La	1.35	1.37	1.13	1.11
Mo	0.57	0.12	0.41	0.44
Nd	4.48	5.14	4.60	4.59
Pr	1.24	1.28	1.14	1.15
Rb	0.38	0.28	0.54	0.51
Se	0.06	<0.10	<0.10	<0.10
Sm	0.93	0.85	0.75	0.76
Sn	0.06	<0.10	<0.10	<0.10
Sr	0.78	0.92	0.81	0.81
Ti	29.46	31.51	33.05	33.12
Y	0.50	0.43	0.38	0.37
Zr	2.21	2.16	1.92	1.94

[a] Te (target wt% = 0.53) was not measured.

volatile Cs and thus, only about 30% of the targeted Cs content remained upon cooling. In contrast, the closed environment in the HIP procedure limits Cs vaporization, and both HIP samples retained approximately 90% of the targeted Cs concentration after processing.[1] It should be noted that the low concentration of remaining Cs in CAF-131 does not preclude melt processing as a feasible fabrication mode for multi-phase ceramics. In our previous work, approximately 68% of the targeted Cs concentration was retained for Fe-doped hollandite processed using a cold crucible induction melter (CCIM) [39]. The increase in Cs retention when compared to earlier work was attributed to the formation of a cold cap and a reduction in surface-to-volume ratio for the scaled-up process, which contribute to the retention of volatile species [40].

Another aspect of the XRD patterns in Fig. 1 is the difference in intensity between the zirconolite and perovskite peaks for the melt-processed and HIPed specimens. For CAF-131, a strong reflection corresponding to zirconolite is clearly evident at a 2θ angle of ~30.4°, while only small peaks indexed to perovskite phases are observed in the sample (as is consistent with the low targeted concentration of 2.54 wt% perovskite in the designed phase assemblage). In contrast, the XRD patterns from HIP-1250 and HIP-1300 show lower intensity peaks from zirconolite and stronger reflections from perovskite phases. In previous research on zirconolite fabricated by a solid-state reaction method, a zirconolite-type phase was formed at temperatures up to 1250 °C, but the XRD analysis also revealed the presence of several perovskite-type phases [24]. Phase-pure zirconolite was subsequently formed only after heating at 1400 °C. Based on the findings of the study, it was suggested that $CaTiO_3$-type structures initially form as intermediate phases in the zirconolite system. Consequently, the presence of strong perovskite peaks and weaker zirconolite reflections in the HIPed samples could be an indicator that the reaction to form zirconolite did not proceed to completion.

Secondary phases (i.e., those not targeted for crystallization) were not identified in the XRD patterns of the melt-processed and HIPed samples. For specimens produced under oxidizing conditions (such as CAF-131), attempts have been made to substitute different divalent and trivalent cations for Ti^{4+} in the hollandite structure with the goal of increasing the tunnel size and facilitating Cs incorporation [11]. However, such substitutions can lead to the formation of both hollandite and water-soluble secondary phases (e.g., $CsAlTiO_4$) [35]. In contrast, octahedrally coordinated Cr^{3+} has the highest crystal field stabilization energy among all geochemically significant $3d^n$ ions [41,42]. Consequently, it is believed that Cr stabilizes the hollandite phase and thus, appears to be an ideal candidate for improving Cs immobilization. The thermal stability of Cr-doped hollandite, and the resulting effect on Cs retention, has been noted in previous work on melt-processed multi-phase ceramics [43].

3.2. SEM-EDS analysis

SEM images acquired for CAF-131, HIP-1250, and HIP-1300 are presented in Fig. 2(a)-(c). The melt-processed sample showed large hollandite grains (darker gray areas) surrounded by zirconolite, pyrochlore, and/or perovskite phases (lighter gray areas). Very small regions with an almost black hue were found to consist primarily of TiO_2. When compared to CAF-131, the HIPed specimens exhibited a more fine-grained microstructure characteristic of a solid-state densification process. Interestingly, raised blackish-gray "islands" of material appeared across the surface of HIP-1300. These

[1] The measured losses in Cs and Mo relative to the formulation were thought to be due to elemental volatilization during calcination.

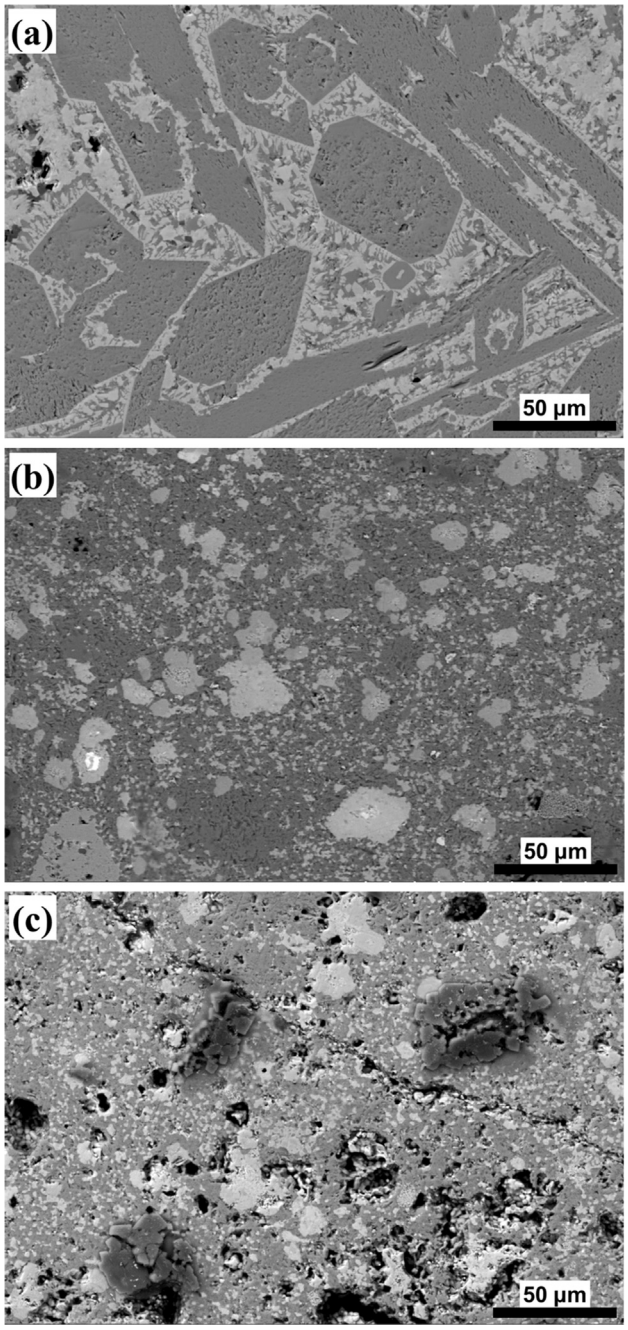

Fig. 2. SEM images of (a) CAF-131, (b) HIP-1250, and (c) HIP-1300.

regions are discussed in more detail below.

To better understand the nature of elemental speciation in the samples, EDS maps were generated for the multi-phase ceramics; the results obtained for CAF-131 are presented in Fig. 3. The Ba and Ti elemental maps clearly indicate the formation of large hollandite grains. Furthermore, Cr, Al, and Fe are not homogeneously distributed within the hollandite. In particular, higher concentrations of Cr are observed at the interior of many hollandite grains, while Al and Fe are found in higher amounts closer to the grain boundaries. This is demonstrated in Table 3, which shows the measured elemental concentrations at different points within the hollandite grains of CAF-131. While the crystallization process for a given oxide system becomes more complex as additional components are introduced, the gradient in Cr, Al, and Fe concentrations could be attributed to the melting points of the respective metal oxides. As pure metal oxides, Cr_2O_3, Al_2O_3, and Fe_2O_3 have melting points of 2432, 2053, and 1539 °C, respectively [44]. Upon cooling from a melt, it is possible that Cr-rich regions crystallize into the hollandite phase first due to the higher melting point of Cr_2O_3. Ideally, a significant portion of the Cs will be immobilized at this point. The remaining liquid in the system is then deficient in Cr and, upon cooling to a suitably low temperature, the crystallization of hollandite rich in Al and Fe occurs.

Another notable feature of CAF-131 was the close correspondence among Ca, Zr, and Nd in the elemental maps. An analysis of 4 different areas showed that the primary elements in these regions were Ti (62.8 ± 0.31 at%), Nd (10.7 ± 0.44 at%), Ca (9.8 ± 0.55 at%), Zr (7.6 ± 0.45 at%), and Fe (5.1 ± 0.27 at%). In the zirconolite structure, Ca^{2+} or Zr^{4+} can be substituted by Nd^{3+}, with the former being preferable due to the smaller disparity in ionic radii between Ca^{2+} and Nd^{3+} [24]. In the case of Ca^{2+} substitution by Nd^{3+}, charge compensation can occur by either trivalent cation substitution at Zr^{4+}/Ti^{4+} sites or via metal vacancy formation at Ca^{2+}/Zr^{4+} positions [21]. Furthermore, extensive Nd substitution into the zirconolite structure leads to partitioning into pyrochlore and/or perovskite phases. The EDS results suggest a scenario whereby Nd may be incorporated into zirconolite, with Fe^{3+} serving as a compensating ion to preserve charge neutrality. Upon exceeding the concentration limit of Nd in zirconolite, perovskite and pyrochlore phases containing Ca and Nd are then formed.

The elemental maps generated for HIP-1250 and HIP-1300 are provided in Fig. 4(a) and (b), respectively. When comparing the EDS results with those acquired for CAF-131, differences are evident. One of the more obvious features is the appearance of dark, raised "islands" when the HIP temperature was raised to 1300 °C. An EDS analysis conducted at 4 different regions showed the composition of some islands to be rich in Cs (58 ± 3.6 at%) and Ti (29 ± 2.4 at%), indicating the possible formation of water-soluble cesium titanate phases. The presence of a Cs-Ti phase is in agreement with the results of earlier work, where it was suggested that partial melting at HIP temperatures of 1300–1350 °C results in Cs partitioning between hollandite and a water-soluble intergranular melt phase [35]. There also appears to be a correspondence between Fe and Mo at several locations for HIP-1250 and HIP-1300, implying the formation of Fe-Mo compounds. While an EDS analysis of these areas revealed no consistent Fe:Mo ratio, the concentrations of other metallic elements in these regions (aside from Fe and Mo) were generally low (<5 at%). The varying Fe:Mo ratio across the examined regions could be due to phase/sample/beam interactions and thus, a more in-depth investigation of Fe-Mo speciation in HIPed multi-phase ceramics is warranted. It must be mentioned that a significant contrast in Mo loss was observed among the samples; approximately 72% and 77% of the targeted Mo concentration was retained in HIP-1250 and HIP-1300, respectively, while only ~21% of the targeted Mo content was measured in CAF-131. As in the case of Cs described earlier, the low percentage of Mo retained in CAF-131 can be attributed to the volatility of MoO_3, which sublimates above 700 °C [45].

Also noteworthy is the difference in Ca-Nd-Zr speciation between the melt-processed and HIP samples. As stated above, many regions of CAF-131 were found to contain Ca, Nd, and Zr in comparable concentrations. In contrast, the EDS maps in Fig. 4 indicate that higher concentrations of Zr are found in more localized regions across the HIPed samples. For HIP-1250, the Ti and Zr contents in some areas were found to be 47.0 ± 2.0 at% and 29.9 ± 2.1 at%, respectively (average of 3 measurements); the remaining components were primarily Fe (11.0 ± 0.6 at%), Nd (7.7 ± 0.3 at%), and Ca (4.4 ± 0.5 at%). However, other regions of HIP-1250 contained very high concentrations of Zr (89.6 ± 0.7 at%, average of 3

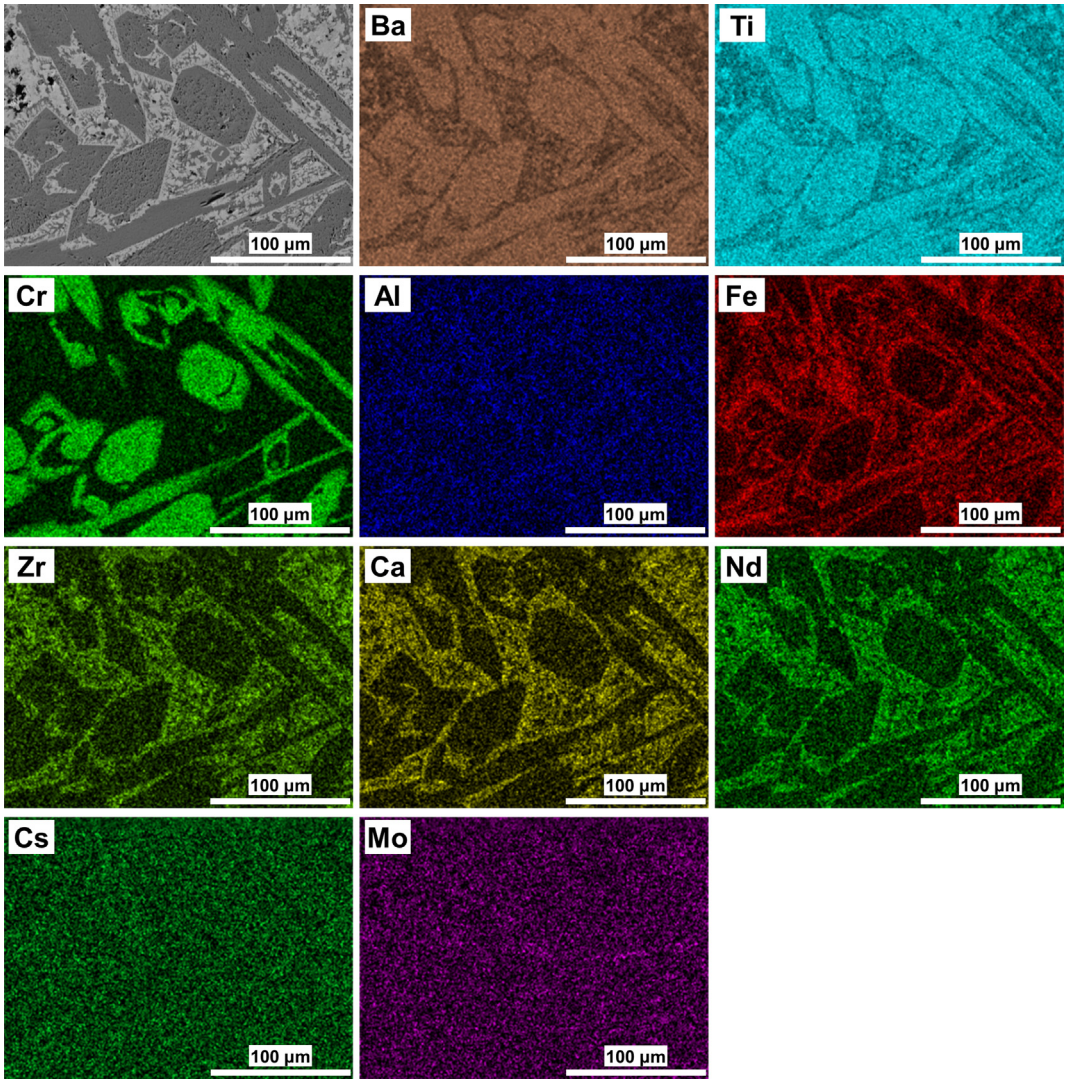

Fig. 3. SEM image (top left) and corresponding EDS elemental maps obtained for CAF-131.

Table 3
Elemental concentrations within CAF-131 hollandite grains.

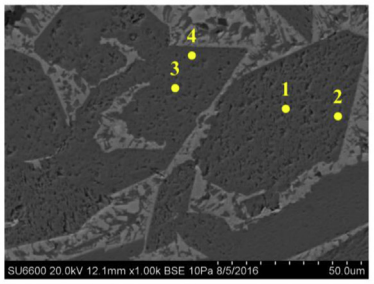

Spot and Primary Elemental Concentrations							
1		2		3		4	
Element	at%	Element	at%	Element	at%	Element	at%
Ti	58.4	Ti	64.3	Ti	56.5	Ti	63.4
Cr	23.1	Fe	15.3	Cr	25.8	Fe	13.3
Ba	12.2	Ba	10.6	Ba	11.6	Ba	10.7
Fe	3.4	Al	4.6	Fe	2.8	Cr	6.1
Al	1.5	Cr	2.9	Al	1.6	Al	4.3
Cs	0.2	Cs	1.0	Cs	0.0	Cs	0.7

measurements) with only minor amounts of Ti (7.7 ± 0.2 at%). An extensive analysis of the HIP-1250 XRD patterns was unable to conclusively identify any compounds such as $(Zr,Ti)O_4$ or ZrO_2 polymorphs, which suggests that these and similar oxides, if present, do not represent a significant portion of the phase assemblage as a whole.

In the HIP-1300 specimen, areas with a Zr content reflective of Zr-Ti-O compounds were not readily observed; an analysis of five regions yielded average Ti and Zr concentrations of 47.1 ± 1.8 at% and 28.1 ± 3.1 at%, respectively; Fe (9.0 ± 0.6 at%), Nd (7.0 ± 0.9 at%), and Ca (3.7 ± 0.4) were also detected. The absence of localized areas with higher Zr content in HIP-1300 can be explained by the higher

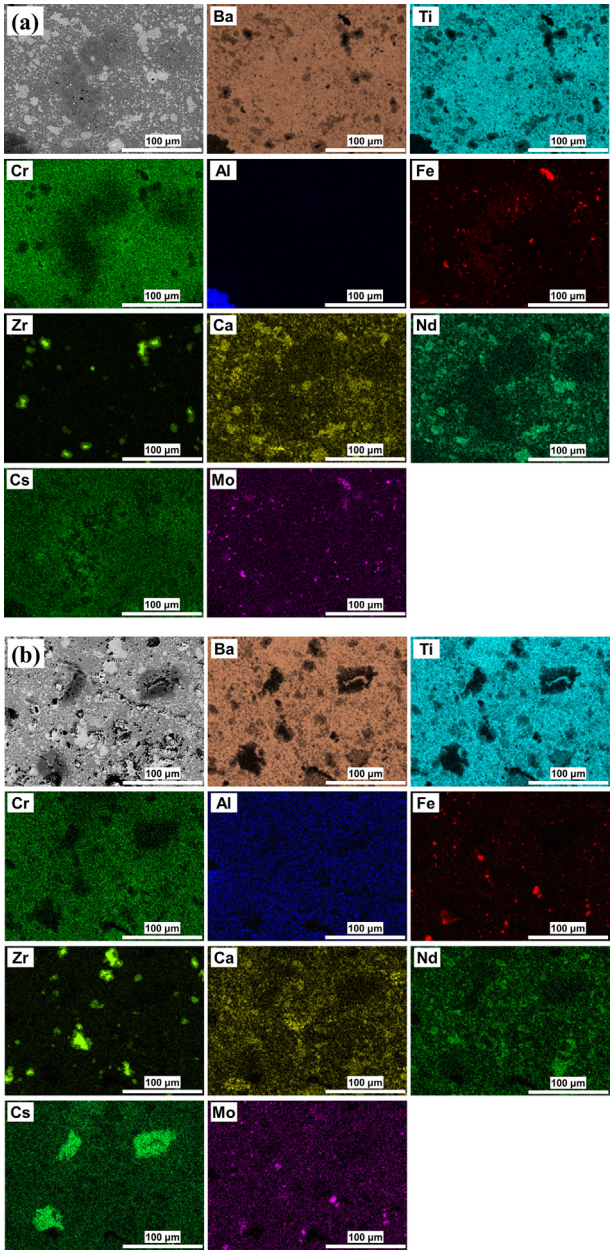

Fig. 4. EDS elemental maps obtained for (a) HIP-1250 and (b) HIP-1300.

processing temperatures needed to form zirconolite when dry metal oxide/carbonate mixtures are utilized rather than metal alkoxides.

In previous research, HIP temperatures of 1280–1320 °C were employed to form the zirconolite phase from mixtures of metal oxides [46,47]. Lowering of the HIP temperature is typically achieved through the use of metal alkoxide/nitrate mixtures that are subsequently dried and calcined prior to the HIP treatment. Such a process improves intermixing of the elemental components and lowers the diffusion distance necessary to form a desired phase assemblage [48]. However, when considering the large-scale production of ceramic waste forms, preparation procedures that involve metal alkoxides are less practical due to their higher cost and sensitivity to moisture [49,50]. With the CAF-131 feed stock prepared in this work, it appears that a HIP temperature of 1300 °C is still insufficient to form appreciable amounts of zirconolite and thus, the resulting phase assemblage included a greater proportion of doped perovskite.

3.3. XPS results

The Cs 3*d* XPS spectra obtained for CAF-131, HIP-1250, and HIP-1300 are displayed in Fig. 5; experimental data in the deconvoluted region are represented by small open circles, while fits to the peaks appear in red. Deconvolution of the spectra was performed using a $3d_{5/2}$:$3d_{3/2}$ peak area ratio of 3:2 and a doublet binding energy separation of 13.94 eV [51]. As evident in Fig. 5, deconvolution and fitting of the CAF-131 XPS spectrum revealed one spin-orbit pair with a Cs $3d_{5/2}$ component positioned at 724.18 eV. The absence of additional peaks indicates that Cs is occupying one specific lattice position. In contrast, photoemission spectra for the HIPed samples contained multiple spin-orbit pairs; the doublets of highest binding energy for HIP-1250 and HIP-1300 (blue lines in Fig. 5) have Cs $3d_{5/2}$ components located at 724.13 and 724.34 eV, respectively. These high binding energy doublets, the positions of which are less than 0.2 eV from that of the single spin-orbit pair from CAF-131, represented the maximum contribution to the total atomic percentage of Cs in the HIPed samples (HIP-1250: 96.8 at%, HIP-1300: 53.1 at%). When considering the strong intensity of hollandite peaks in the XRD patterns of the melt-processed and HIPed samples (see Fig. 1), it is likely that the Cs $3d_{5/2}$ components around 724 eV for all specimens are associated with Cs in 8-fold coordinated tunnel sites of the hollandite lattice. For HIP-1250 and HIP-1300, lower binding energy doublets (green lines in Fig. 5) with Cs $3d_{5/2}$ components positioned at 722.40 and 722.61 eV, respectively, were also detected. An additional low binding energy spin-orbit pair with a Cs $3d_{5/2}$ component situated at 720.75 eV (orange line) was identified in the HIP-1300 sample. While the exact origins of the low binding energy doublets in the HIPed specimens have not yet been elucidated, islands rich in Cs and Ti were observed on the surface of HIP-1300. Such compounds are known to possess an open framework structure from which Cs can easily be leached [35,52].

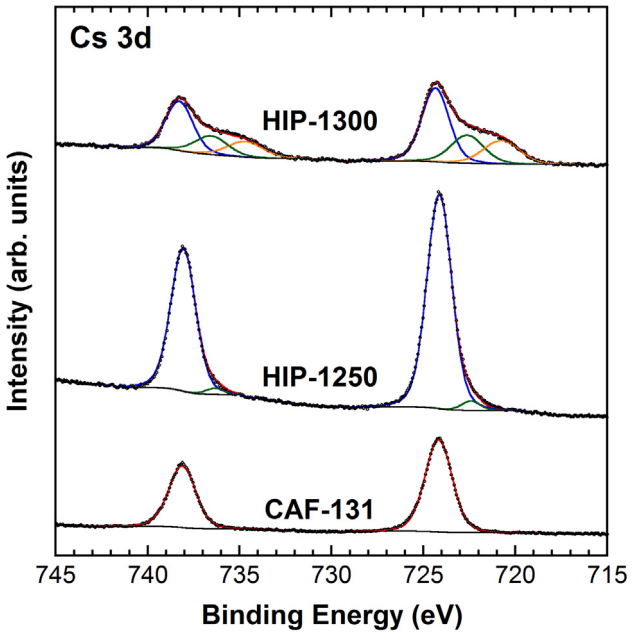

Fig. 5. Cs 3*d* XPS spectra obtained for CAF-131, HIP-1250, and HIP-1300. Experimental data in the deconvoluted region are denoted by open black circles, while fits to the spectra are represented by red lines. (For interpretation of the references to colour in this figure legend, the reader is referred to the Web version of this article.)

3.4. Leach testing

Although measurements were made to quantify leachate concentrations for all elements in the batch composition (with the exception of Te), the majority were below instrumental detection limits (<100 ppb Al and Ca, <10 ppb Ti, <20 ppb Fe, <1 ppb Cr, Y, Zr, Cd, Sn, Se, Te, La, Ce, Pr, Nd, Sm, and Eu, and Gd) and thus, only measurable elemental release concentrations will be discussed. The fractional release rates of Cs, Rb, Ba, and Sr for CAF-131, HIP-1250, and HIP-1300 are displayed in Fig. 6(a)-(d), respectively. While the HIP-1250 sample exhibits lower Cs and Rb fractional release rates than those observed for HIP-1300, both HIP specimens show higher alkali metal release rates when compared to CAF-131. The relatively poor Cs leach characteristics of HIP-1300 are believed to be due to the high HIP temperature, which led to partial melting and the formation of water-soluble Cs compounds. The enhanced leaching of Cs in HIP-1300 is also in agreement with the XPS findings presented earlier, where a Cs 3*d* doublet appeared at a binding energy more than 3.5 eV lower than that corresponding to hollandite. Although the Ba fractional release rates for CAF-131 and HIP-1250 are quite comparable, a sizable increase in the fraction of Sr release was noted for CAF-131 when compared to those of the HIP specimens. Considering the XRD findings in Fig. 1, it can be implied that Sr is effectively immobilized in perovskite phases formed during the HIPing.

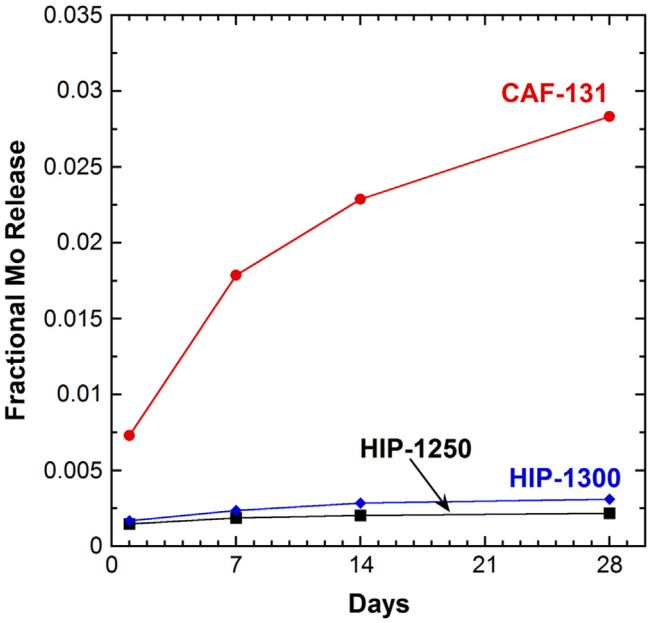

Fig. 7. Fractional release of Mo for CAF-131, HIP-1250, and HIP-1300 over 28 days.

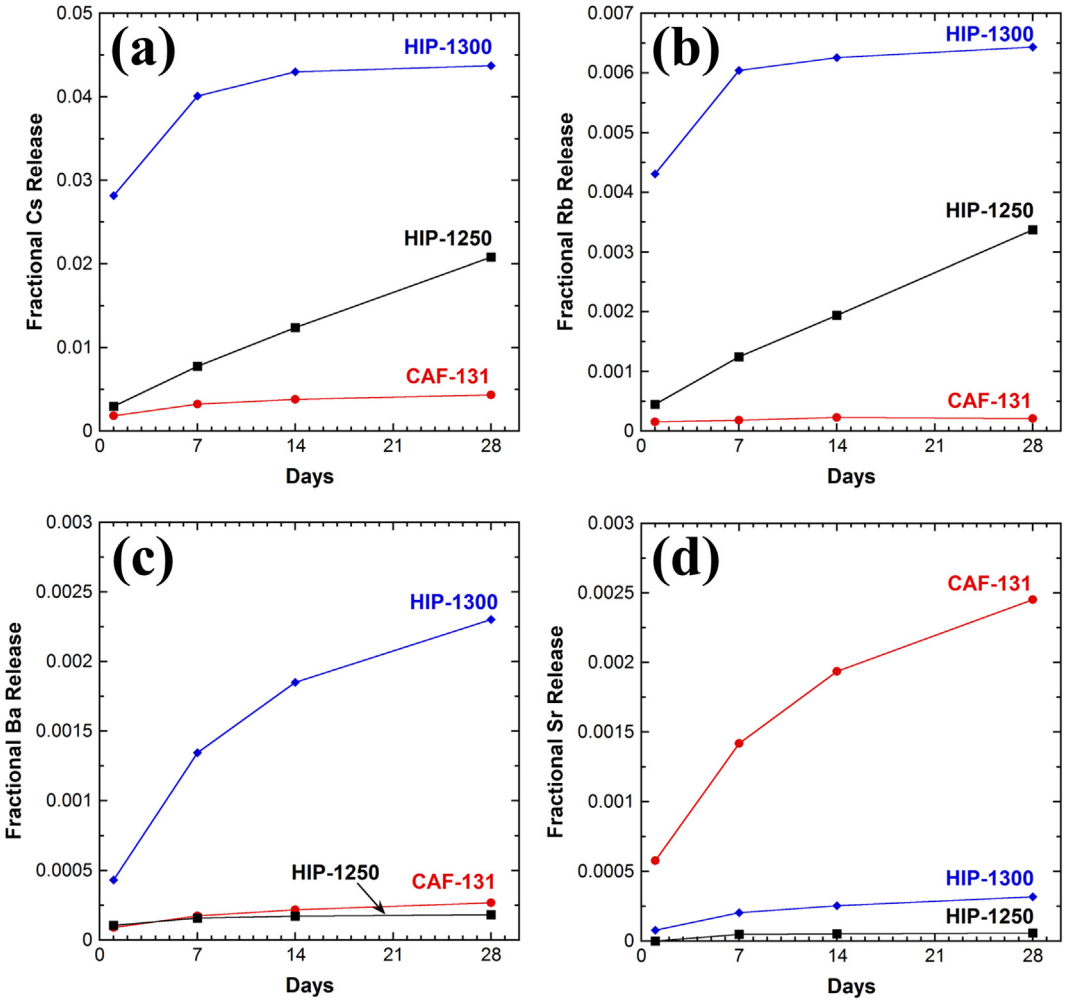

Fig. 6. Fractional release rates of (a) Cs, (b) Rb, (c) Ba, and (d) Sr for CAF-131, HIP-1250, and HIP-1300.

Fractional release rates for Mo in CAF-131, HIP-1250, and HIP-1300 are displayed in Fig. 7. It is apparent that Mo retention is greatly enhanced in the HIP samples. As stated previously, a correspondence between Fe and Mo was observed in the EDS data obtained for both HIPed specimens. The formation of an Fe-Mo compound during the HIP treatment may serve to limit the leaching of Mo in the multi-phase ceramics. Examining the leach test data as a whole, it can be inferred that an increase in the fractional release of alkali metals from HIPed specimens with the targeted CAF-131 hollandite composition could be due to the delicate balance that exists between the use of sufficiently high HIP temperatures (to produce the proper phase assemblage) and the avoidance of water-soluble compound formation at such temperatures.

4. Conclusions

Multi-phase ceramic waste forms were produced via melt-processing and HIP procedures. To facilitate a direct comparison of the fabrication protocols, a composition with a target hollandite stoichiometry of $Ba_{1.0}Cs_{0.3}\mathbf{Cr}_{1.0}\mathbf{Al}_{0.3}\mathbf{Fe}_{1.0}Ti_{5.7}O_{16}$ (CAF-131) was manufactured by each method. For HIP samples processed at 1250 and 1300 °C, high-intensity peaks from hollandite and perovskite phases were present along with low-intensity reflections from zirconolite/pyrochlore. Considering previous work showing perovskite as an intermediate phase during zirconolite formation, incomplete crystallization of zirconolite likely occurred in the HIP process. Regarding the morphology of the samples, crystallization from a melt yielded microstructures with large hollandite grains, while the HIP samples exhibited more fine-grained morphologies characteristic of a solid-state densification process. Elemental speciation of Cr, Fe, and Al was apparent within the melt-processed CAF-131 hollandite grains, which presented Cr “cores” surrounded by Fe and Al closer to the grain boundaries. Such a phenomenon was attributed to a fractional crystallization process due to the melting points of the respective component oxides. A close correspondence between Ca, Zr, and Nd was noted in CAF-131, suggesting the formation of doped zirconolite/pyrochlore phases. In contrast, Zr was detected in more localized regions across the surfaces of the HIPed specimens. The surface of HIP-1300 also contained “islands” of material rich in Cs. The presence of these islands could be related to the appearance of a lower binding energy Cs 3*d* doublet that was only observed for HIP-1300.

28-day leach tests were carried out to investigate the durability of the multi-phase ceramics. The fractional release of Cs and Rb from CAF-131 was lower than that detected for both HIP samples. However, the release rate for Sr was higher in CAF-131 when compared to those from HIPed specimens. The retention of Mo was found to be greater in HIP-1250 and HIP-1300 when compared to that for CAF-131. Such a finding may be attributed to the formation of Fe-Mo compounds in the HIP samples. In future research, the relative ratio of targeted phases in melt-processed multi-phase ceramics with CAF-131 hollandite compositions will be varied so as to optimize the leach behavior.

Conflicts of interest

None.

Acknowledgements

The authors gratefully acknowledge technical contributions from Phyllis Workman and David Missimer at SRNL for assistance with sample preparation and property measurements. Financial support from the US DOE Fuel Cycle R&D program and Materials Recovery and Waste Form Development (MRWFD) Campaign under the direction of Terry Todd (National Technical Director), John Vienna (Deputy Manager), and Kimberly Gray (DOE Federal Manager) is also acknowledged. The authors are grateful to Stavros Karakalos at the University of South Carolina for his assistance in obtaining XPS data, D. Gregg for comments on the manuscript, and N. Webb for HIPing. Work conducted at Savannah River National Laboratory was supported by the U.S. DOE under contract number DE-AC09-08SR22470.

References

[1] W.J. Weber, A. Navrotsky, S. Stefanovsky, E.R. Vance, E. Vernaz, Materials science of high-level nuclear waste immobilization, MRS Bull. 34 (2009) 46–53.
[2] J. Crum, V. Maio, J. McCloy, C. Scott, B. Riley, B. Benefiel, J. Vienna, K. Archibald, C. Rodriguez, V. Rutledge, Z. Zhu, J. Ryan, M. Olszta, Cold crucible induction melter studies for making glass ceramic waste forms: a feasibility assessment, J. Nucl. Mater. 444 (2014) 481–492.
[3] A.E. Ringwood, S.E. Kesson, N.G. Ware, W.O. Hibberson, A. Major, The SYNROC process: a geochemical approach to nuclear waste immobilization, Geochem. J. 13 (1979) 141–165.
[4] I.W. Donald, Waste Immobilization in Glass and Ceramic Based Hosts: Radioactive, Toxic and Hazardous Wastes, Wiley, West Sussex, 2010.
[5] A.E. Ringwood, Disposal of high-level nuclear wastes: a geological perspective, Mineral. Mag. 49 (1985) 159–176.
[6] A.E. Ringwood, S.E. Kesson, N.G. Ware, W. Hibberson, A. Major, Immobilisation of high level nuclear reactor wastes in SYNROC, Nature 278 (1979) 219–223.
[7] I.A. Sobolev, F.A. Lifanov, S.V. Stefanovsky, S.A. Dmitriev, Development of Synroc Melting Process, Waste Management, Tucson, AZ, 1995, pp. 1–9.
[8] I.A. Sobolev, S.V. Stefanovsky, B.I. Omelianenko, S.V. Ioudintsev, Comparative study of Synroc-C ceramics produced by hot-pressing and inductive melting, Mater. Res. Soc. Symp. Proc. 465 (1996) 371–378.
[9] S.E. Kesson, T.J. White, $[Ba_xCs_y][(Ti,Al)^{3+}_{2x+y}Ti^{4+}_{8-2x-y}]O_{16}$ Synroc-type hollandites I. Phase chemistry, Proceedings of the Royal Society of London Series A-Mathematical Physical and Engineering Sciences 405 (1986) 73–101.
[10] H. Miura, The crystal structure of hollandite, Mineral. J. 13 (1986) 119–129.
[11] V. Aubin-Chevaldonnet, D. Caurant, A. Dannoux, D. Gourier, T. Charpentier, L. Mazerolles, T. Advocat, Preparation and characterization of $(Ba,Cs)(M,Ti)_8O_{16}$ ($M = Al^{3+}$, Fe^{3+}, Ga^{3+}, Cr^{3+}, Sc^{3+}, Mg^{2+}) hollandite ceramics developed for radioactive cesium immmobilization, J. Nucl. Mater. 366 (2007) 137–160.
[12] A.Y. Leinekugel-Le-Coeq, P. Deniard, S. Jobic, R. Cerny, F. Bart, H. Emerich, Synthesis and characterization of hollandite-type material intended for the specific containment of radioactive cesium, J. Solid State Chem. 179 (2006) 3196–3208.
[13] G.C.C. Costa, H.W. Xu, A. Navrotsky, Thermochemistry of barium hollandites, J. Am. Ceram. Soc. 96 (2013) 1554–1561.
[14] R.C. Ewing, W.J. Weber, J. Lian, Nuclear waste disposal-pyrochlore ($A_2B_2O_7$): nuclear waste form for the immobilization of plutonium and "minor" actinides, J. Appl. Phys. 95 (2004) 5949–5971.
[15] G.R. Lumpkin, Ceramic waste forms for actinides, Elements 2 (2006) 365–372.
[16] B.P. Mandal, A.K. Tyagi, Pyrochlores: potential multifunctional materials, BARC Newsletter 6 (2010).
[17] A. Salamat, P.F. McMillan, S. Firth, K. Woodhead, A.L. Hector, G. Garbarino, M.C. Stennett, N.C. Hyatt, Structural transformations and disordering in zirconolite ($CaZrTi_2O_7$) at high pressure, Inorg. Chem. 52 (2013) 1550–1558.
[18] G.R. Lumpkin, B.D. Begg, K.L. Smith, Radiation Damage Effects in Pyrochlore and Zirconolite Ceramic Matrices for the Immobilization of Actinide-rich Wastes, 2000, p. 575. Scientific research on the back-end of the fuel cycle for the 21 century, France.
[19] G.R. Lumpkin, K.R. Whittle, C.J. Howard, Z. Zhang, F.J. Berry, G. Oates, C.T. Williams, A.N. Zaitsev, Crystal chemistry and cation ordering in zirconolite 2M, Mater. Res. Soc. Symp. Proc. 932 (2006) 53.
[20] D. Caurant, P. Loiseau, I. Bardez, Structural characterization of Nd-doped Hf-zirconolite $Ca_{1-x}Nd_xHfTi_{2-x}Al_xO_7$ ceramics, J. Nucl. Mater. 407 (2010) 88–99.
[21] A.A. Coelho, R.W. Cheary, K.L. Smith, Analysis and structural determination of Nd-substituted zirconolite-4M, J. Solid State Chem. 129 (1997) 346–359.
[22] B.M. Clark, S.K. Sundaram, S.T. Misture, Polymorphic transitions in cerium-substituted zirconolite ($CaZrTi_2O_7$), Sci. Rep. 7 (2017) 5920.
[23] M.A. Peña, J.L.G. Fierro, Chemical structures and performance of perovskite oxides, Chem. Rev. 101 (2001) 1981–2018.
[24] M. Jafar, P. Sengupta, S.N. Achary, A.K. Tyagi, Phase evolution and microstructural studies in $CaZrTi_2O_7$-$Nd_2Ti_2O_7$ system, J. Am. Ceram. Soc. 97 (2014) 609–616.
[25] M.L. Carter, A.L. Gillen, K. Olufson, E.R. Vance, HIPed tailored hollandite waste forms for the immobilization of radioactive Cs and Sr, J. Am. Ceram. Soc. 92 (2009) 1112–1117.
[26] J. Amoroso, J.C. Marra, M. Tang, Y. Lin, F.L. Chen, D. Su, K.S. Brinkman, Melt processed multiphase ceramic waste forms for nuclear waste immobilization, J. Nucl. Mater. 454 (2014) 12–21.
[27] W.E. Lee, M.I. Ojovan, M.C. Stennett, N.C. Hyatt, Immobilisation of radioactive

waste in glasses, glass composite materials and ceramics, Adv. Appl. Ceram. 105 (2006) 3–12.
[28] J. Amoroso, J. Marra, S.D. Conradson, M. Tang, K. Brinkman, Melt processed single phase hollandite waste forms for nuclear waste immobilization: $Ba_{1.0}Cs_{0.3}A_{2.3}Ti_{5.7}O_{16}$; A = Cr, Fe, Al, J. Alloy. Comp. 584 (2014) 590–599.
[29] J.W. Amoroso, J.C. Marra, Development of Melt Processed Ceramics for Nuclear Waste Immobilization, SRNL-STI-2014-00467, Savannah River National Laboratory, Aiken, SC, 2014.
[30] K.S. Brinkman, J. Amoroso, J.C. Marra, Crystalline Ceramic Waste Forms: Comparison of Reference Process for Ceramic Waste Form Fabrication, SRNL-STI-2013–20100442, FCRD-SWF-2013-000229, Savannah River National Laboratory, Aiken, SC, 2013.
[31] K.S. Brinkman, K.M. Fox, J.C. Marra, M. Tang, Crystalline Ceramic Waste Forms: Reference Formulation Report, SRNL-STI-2012–20100281, FCRD-SWF-2012-000116, Savannah River National Laboratory, Aiken, SC, 2012.
[32] Committee on Waste Forms Technology and Performance, Waste Forms Technology and Performance: Final Report, The National Academies Press, Washington, DC, 2011.
[33] Y.H. Hsieh, D. Horlait, S. Humphry-Baker, E.R. Vance, D.J. Gregg, L. Edwards, T.D. Waite, W.E. Lee, Wasteforms for waste from advanced reprocessing, MRS Adv 1 (2017) 4255–4260.
[34] A. Jostsons, K.D. Reeve, Immobilization of high level waste in SYNROC, Trans. Am. Nucl. Soc. 56 (1988) 537–544.
[35] S.E. Kesson, The immobilization of cesium in synroc hollandite, Radioact. Waste Manag. Nucl. Fuel Cycle 4 (1983) 53–72.
[36] ASTM International, ASTM C1220–10: Standard Test Method for Static Leaching of Monolithic Waste Forms for Disposal of Radioactive Waste, West Conshohocken, PA, 2010.
[37] Y. Xu, M. Feygenson, K. Page, L.S. Nickles, K.S. Brinkman, Structural evolution in hollandite solid solutions across the a-site compositional range from $Ba_{1.33}Ga_{2.66}Ti_{5.34}O_{16}$ to $Cs_{1.33}Ga_{1.33}Ti_{6.67}O_{16}$, J. Am. Ceram. Soc. 99 (2016) 4100–4106.
[38] Y. Xu, Y. Wen, R. Grote, J. Amoroso, L.S. Nickles, K.S. Brinkman, A-site compositional effects in Ga-doped hollandite materials of the form $Ba_xCs_{y-}Ga_{2x+y}Ti_{8-2x-y}O_{16}$: implications for Cs immobilization in crystalline ceramic waste forms, Sci. Rep. 6 (2016) 8.
[39] J.W. Amoroso, J. Marra, C.S. Dandeneau, K. Brinkman, Y. Xu, M. Tang, V. Maio, S.M. Webb, W.K.S. Chiu, Cold crucible induction melter test for crystalline ceramic waste form fabrication: a feasibility assessment, J. Nucl. Mater. 486 (2017) 283–297.
[40] N.E. Bibler, T.L. Fellinger, S.L. Marra, R.J. O'Driscoll, J.W. Ray, W.T. Boyce, Tc-99 and Cs-137 volatility from the DWPF production melter during vitrification of the first macrobatch of HLW sludge at the Savannah River Site, Mater. Res. Soc. Symp. Proc. 608 (2000).
[41] R.G. Burns, Crystal field effects in chromium and its partitioning in the mantle, Geochem. Cosmochim. Acta 39 (1975) 857–864.
[42] K. Langer, M. Andrut, The crystal field concept (CFC) in geosciences: does the crystal field stabilization energy of Cr3+rule its intercrystalline partitioning behavior?, in: M.D. Dyar, C. McCammon, M.W. Schaefer (Eds.), Mineral Spectroscopy: a Tribute to Roger G. Burns, The Geochemical Society Special Publication, Geochemical Society, Houston, USA, 1996, pp. 29–40.
[43] P. Tumurugoti, S.K. Sundaram, S.T. Misture, J.C. Marra, J. Amoroso, Crystallization behavior during melt-processing of ceramic waste forms, J. Nucl. Mater. 473 (2016) 178–188.
[44] W.M. Haynes, CRC Handbook of Chemistry and Physics, 97th ed., CRC Press, 2016.
[45] R.C. Ropp, Encyclopedia of the Alkaline Earth Compounds, Elsevier Science, Oxford, UK, 2012.
[46] J. Squire, E.R. Maddrell, N.C. Hyatt, M.C. Stennett, Influence of lubricants and attrition milling parameters on the quality of zirconolite ceramics, consolidated by hot isostatic pressing, for immobilization of plutonium, Int. J. Appl. Ceram. Technol. 12 (2015) E92–E104.
[47] Y. Zhang, M.W.A. Stewart, H. Li, M.L. Carter, E.R. Vance, S. Moricca, Zirconolite-rich titanate ceramics for immobilisation of actinides – waste form/HIP can interactions and chemical durability, J. Nucl. Mater. 395 (2009) 69–74.
[48] E. Maddrell, Hot isostatically pressed wasteforms for future nuclear fuel cycles, Chem. Eng. Res. Des. 91 (2013) 735–741.
[49] A.E. Danks, S.R. Hall, Z. Schnepp, The evolution of 'sol-gel' chemistry as a technique for materials synthesis, Mater. Horiz. 3 (2016) 91–112.
[50] M.N. Rahaman, Ceramic Processing, Taylor & Francis, New York, 2006.
[51] J.F. Moulder, W.F. Stickle, P.E. Sobol, K.D. Bomben, Handbook of X-ray Photoelectron Spectroscopy, Perkin-Elmer Corp., Eden Prarie, MN, 1992.
[52] B.M. Gatehouse, Structure of $CsAlTiO_4$ - a compound with TiO_4 tetrahedra, Acta Cryst. C C45 (1989) 1674–1677.